Optics Letters

Elliptical polarization in VCSELs via joint interaction of a tilted sub-wavelength grating and intrinsic semiconductor anisotropies

Valerio Torrelli,[1,2] Lorenzo Miri,[1,*] Martino D'Alessandro,[1,2] Alberto Gullino,[2] Michael Zimmer,[3] Katharina Dahler,[3] Michael Jetter,[3] Peter Michler,[3] Wolfgang Elsäßer,[2,4,5] Francesco Bertazzi,[1] Alberto Tibaldi,[1] and Pierluigi Debernardi[2]

[1] Department of Electronics and Telecommunications (DET), Politecnico di Torino, Corso Duca degli Abruzzi, 24, Torino 10129, Italy
[2] Istituto di Elettronica e di Ingegneria dell'Informazione e delle Telecomunicazioni (IEIIT) del Consiglio Nazionale delle Ricerche (CNR), Politecnico di Torino, Italy
[3] Institut für Halbleiteroptik und Funktionelle Grenzflächen, Center for Integrated Quantum Science and Technology (IQST) and Research Center SCoPE, Universität Stuttgart, Allmandring 3 Stuttgart 70569, Germany
[4] Institute of Applied Physics, Technische Universität Darmstadt, Schlossgartenstrasse 7 Darmstadt 64289, Germany
[5] School of Physics, Trinity College Dublin, Dublin 2, Ireland
*lorenzo.miri@polito.it

Received 27 January 2025; revised 7 April 2025; accepted 7 April 2025; posted 8 April 2025; published 1 May 2025

We demonstrate numerically and experimentally that, in vertical-cavity surface-emitting lasers (VCSELs), a non-chiral cavity can be converted into a chiral one by the interaction between a sub-wavelength grating tilted with respect to the crystalline axes and the intrinsic semiconductor optical anisotropies, thus enabling the emission of elliptically polarized light. The measured Stokes parameters of such a VCSEL, realized by a standard grating based VCSEL fabricati on process, are in line with the modeling results. We demonstrate through simulations that a degree of circular polarization of 0.9 can be obtained by varying the grating parameters. The full Poincaré sphere is accessible on demand if mechanical strain is also considered.

https://doi.org/10.1364/OL.557703

Introduction. In recent years, vertical-cavity surface-emitting lasers (VCSELs) have become the predominant coherent light sources for a variety of established applications, such as short-haul optical interconnects [1,2] and 3D sensing [3]. However, even though VCSELs were originally appealing for their reduced power consumption, a demand for high-power single-mode VCSELs arose from novel applications such as LiDAR and devices based on optical atomic pumping [4]. The latter represents a class of devices including quantum gyroscopes [5,6], atomic clocks [7], and atomic magnetometers [8], relying on more compact light sources such as VCSELs to scale down their size to the chip scale [9]. Typical requirements for the laser source are high-power single transverse mode with a stable linear polarization in output [10,11]. State-of-the-art VCSELs are currently able to emit a stable linear polarization due to the introduction of gratings [12], making them a suitable candidate for such new applications. However, atomic devices also require circularly polarized (CP) light, needed to excite the required atomic transitions [9]. This is currently achieved by the usage of a quarter-wave plate to convert the VCSEL output polarization from linear to circular. This limits the scale-down of atomic devices, raising the need for native CP emitters. In the VCSEL field, various possibilities to achieve such a result are investigated in [13], focusing on 3D cavity chirality via the introduction of misaligned optical anisotropies. In this work, we aim to harness the capabilities of sub-wavelength grating (SWG) VCSELs to inherently emit different polarization states by tilting the grating bars with respect to the crystalline axis of the device. Building on the model outlined in [13], we investigated the combined effect of intrinsic anisotropies, such as electro- and elasto-optic effects, aligned with the crystalline axes, together with the extrinsic anisotropy introduced by the tilted SWG. The validation of our model through comparison with experimental data opens new possibilities for polarization engineering in standard grating VCSELs, enabling access to a variety of elliptical polarization states.

Structure under investigation. The considered AlGaAs-VCSEL, emitting at $\lambda = 850$ nm, is grown epitaxially by metal-organic vapor-phase epitaxy (MOVPE) on an n-doped GaAs substrate with a donor concentration of $N_D = 2 \times 10^{18}\ \mathrm{cm}^{-3}$. The bottom n-doped ($N_D = 1.5 \times 10^{18}\ \mathrm{cm}^{-3}$) distributed Bragg reflector (DBR) comprises 30 pairs of $Al_{0.10}Ga_{0.90}As$:Si/$Al_{0.95}Ga_{0.05}As$:Si layers. Each layer has a thickness of $\lambda/(4n_r)$, where n_r is its refractive index. Above the bottom DBR, an intrinsic λ-cavity made of $Al_{0.50}Ga_{0.50}As$ embeds the active region (AR), which provides optical gain to support lasing. The top p-doped ($N_A = 1.5 \times 10^{18}\ \mathrm{cm}^{-3}$) DBR consists of 19.5 pairs of $Al_{0.20}Ga_{0.80}As$:Zn/$Al_{0.95}Ga_{0.05}As$:Zn, i.e., 39 alternating layers, connected by a linear molar fraction grading

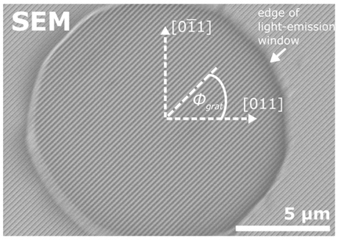

Fig. 1. SEM picture of the light-emission window of a VCSEL. The SWG is tilted by the angle ϕ_{grat}.

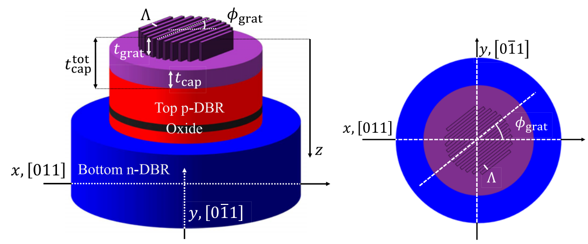

Fig. 2. Sketch of the investigated VCSEL structure, together with the reference system and the definition of the most relevant dimensions.

of 26 nm. Following the cavity, a high aluminum content layer ($Al_{0.98}Ga_{0.02}As$) is introduced for oxidation, allowing the transverse definition of the oxide aperture, which confines both carriers and light.

The out-of-phase top DBR is turned in-phase by a heavily p-doped GaAs cap layer with an acceptor concentration of $N_A = 1 \times 10^{19}\ \text{cm}^{-3}$ and a total thickness of $t_{\text{cap}}^{\text{tot}} = 3\lambda/(4n_r) = 175$ nm, which also serves as the contact layer.

To enable polarization control, a SWG is defined in a first processing step by electron-beam lithography and subsequently etched into the cap layer with a spatial period $\Lambda = 200$ nm by inductively coupled plasma (ICP) etching. The grating extends to a depth of $t_{\text{grat}} = \lambda/(2n_r) = 116$ nm, leaving a residual cap layer thickness of $t_{\text{cap}} = t_{\text{cap}}^{\text{tot}} - t_{\text{grat}} = 59$ nm. In Fig. 1, we show a scanning electron microscope (SEM) image of the resulting SWG. The reference coordinate system is aligned to the crystal directions ($x = [011]$, $y = [0\bar{1}1]$) and the longitudinal z axis opposite to the growth direction. The subsequent device fabrication follows a standard VCSEL process. Mesas are defined by a combination of photolithography and ICP etching. The current confining oxide aperture is formed by wet-thermal oxidation of the $Al_{0.98}$GaAs:Zn layer in an oxidation oven. Thereon, a 4 μm BCB isolation layer is spun on the sample and structured via UV lithography. In the last processing steps, the p-contact is defined by photolithography and deposited by electron-beam evaporation, before evaporation of the n-contact completes the fabrication process.

To investigate the effect of the tilting angle ϕ_{grat} (displayed in Fig. 2) between the crystal axes and the grating bars, many identical samples with different ϕ_{grat} values ranging from 0° to 180° in steps of 5° are manufactured and analyzed, both experimentally and through simulations. This comprehensive approach ensures that the polarization features are thoroughly understood in all conditions. As the device operates in a single transverse mode, a one-dimensional electro-optical simulation along the z axis is sufficient to capture its polarization characteristics. Figure 2 shows a schematic of the structure.

Simulation methodologies. Our SWG VCSEL supports two modes with identical spatial intensity distribution, but different polarizations, with different threshold gains and emission wavelengths. The mode with the lowest threshold is referred to as lasing polarization.

To investigate this problem, a 1D vectorial optical simulation can be performed along the z axis. Our in-house vectorial 1D VCSEL ELectroMagnetic Suite (VELMS) serves as an optical mode solver. It relies on the expansion of the electric field in terms of the basis of the optical modes supported by a reference medium [14]. Here, a simplified basis is considered, still vectorial, yet only considering normal incidence. This approach was also applied in [13]. From the anisotropic refractive index longitudinal profile, one obtains the modal features of the two polarizations in terms of emission wavelengths; threshold gains; standing wave (SW) profiles, i.e., modulus square of the optical field; and electric field phasors, i.e., Jones vectors, at the outcoupling facet of the laser. The Jones vector for the lasing polarization can be written as $\boldsymbol{\mathcal{E}} = \mathcal{E}_x\mathbf{x} + \mathcal{E}_y\mathbf{y}$, $\mathcal{E}_x, \mathcal{E}_y \in \mathbb{C}$. The corresponding Stokes parameters [15,16] are defined as

$$S_0 = |\mathcal{E}_x|^2 + |\mathcal{E}_y|^2, \tag{1a}$$

$$S_1 = \frac{|\mathcal{E}_x|^2 - |\mathcal{E}_y|^2}{S_0} \in [-1, +1], \tag{1b}$$

$$S_2 = \frac{+2\Re\left\{\mathcal{E}_y^*\mathcal{E}_x\right\}}{S_0} \in [-1, +1], \tag{1c}$$

$$S_3 = \frac{-2\Im\left\{\mathcal{E}_y^*\mathcal{E}_x\right\}}{S_0} \in [-1, +1]. \tag{1d}$$

The lasing polarization results from the competition of optical anisotropies, creating a chiral resonator when they are misaligned [13]. In the structure of Fig. 2, two anisotropies are present: the tilted SWG and the electro-optic effect (EOE). VELMS propagates the field in the resonator using the transmission matrices of the layers and imposing the cavity round trip Barkhausen criterion. The transmission matrix of the SWG is computed by the rigorous coupled wave analysis [17,18]. On the other hand, the anisotropy arising from the EOE can be evaluated in terms of the semi-difference of the relative dielectric constants along x, $\epsilon_{xx} = n_{xx}^2$, and y, $\epsilon_{yy} = n_{yy}^2$, as [19]

$$\Delta\epsilon_{\text{EOE}}(z) = \frac{\epsilon_{xx} - \epsilon_{yy}}{2} = n_r^4(z) r_{41}(z) E(z), \tag{2}$$

where $n_r(z)$ is the refractive index profile in the absence of the optical anisotropies induced by the electro-optic and elasto-optic effects, $E(z)$ is the z-component of the electrostatic field profile, and $r_{41} = 1.6$ pm/V for GaAs [20] and 0.78 pm/V for AlAs [21]. Intermediate aluminum molar fractions are linearly interpolated. $E(z)$ is obtained with our in-house 1D drift-diffusion (DD) code [22] and is mainly governed by the doped heterostructures of the DBRs. Finally, if a uniform strain σ (adimensional) is mechanically applied along the crystal axes an additional anisotropy results as a consequence of the elasto-optic effect. The equivalent of Eq. (2) for the elasto-optic effect reads

$$\Delta\epsilon_{\sigma} = n_r^4(z) p_{44} \frac{\sigma}{2}, \tag{3}$$

where $p_{44} = 0.072$ [19]. The overall anisotropy $\Delta\epsilon = \Delta\epsilon_{\text{EOE}} + \Delta\epsilon_{\sigma}$ can be evaluated as the sum of the two effects.

Experimental characterization. The VCSEL characterization setup features a temperature-cooled copper plate that also serves as the n-electrode on which the device under investigation is placed. The p-side of the VCSEL is contacted via a probe needle controlled by a micromanipulator. The setup further uses an optical telescope arrangement consisting of three lenses for collimating and guiding the VCSEL emission toward the measurement head of a Newport 1830-C powermeter. In order to determine the Stokes parameters, the methode of the rotating quarter-wave plate is applied [16,23,24]. For this purpose a quarter-wave plate on an automatized rotation mount and a linear polarizer are inserted into the optical path in front of the powermeter head. A mechanical stop is used to ensure a fixed orientation of the VCSEL chip for all measurements. While the polarizer is kept fixed, the quarter-wave plate is rotated and the intensity on the powermeter head detected. The intensity detected on the powermeter head in dependence of the quarter-wave plate rotation angle θ follows

$$I = \frac{1}{2}\left(A + B\sin(2\theta) + C\cos(4\theta) + D\sin(4\theta)\right), \tag{4}$$

where the Stokes parameters S_0, S_1, S_2 and S_3 are obtained from according to

$$S_0 = A - C,\ S_1 = 2C,\ S_2 = 2D,\ S_3 = B. \tag{5}$$

Results and discussion. The structure reported in Fig. 2 is simulated by means of our DD model. Its band diagram under an applied bias voltage of 3 V is reported in Fig. 3. We sketch with different colors the longitudinal extension of the cap layer, the p-DBR, the cavity, the n-DBR, and the substrate, from left to right. The electrostatic field distribution is characterize by strong peaks at the hetero-interfaces of the DBR (mitigated in the top p-DBR by the compositional grading) and is independent from the applied voltage. This profile induces an EOE anisotropy that depends solely on the aluminum molar fraction and doping profiles. As a result, the emitted polarization is unaffected by the DC bias point. At this stage, optical simulations can be carried out. Before incorporating the grating effects, we focus exclusively on the EOE using Eq. (2). The resulting SW can be superimposed with the anisotropy profile, $\Delta\epsilon_{\mathrm{EOE}}$, as shown in Fig. 4. This analysis is important for understanding the significant impact of the EOE on device performance. Despite the null average of $E(z)$, the positive peaks within the DBRs are aligned with the nodes of the SW and, consequently, minimally interact with the optical mode. Conversely, negative peaks coincide with the antinodes of the SW, resulting in an averaged anisotropy calculated as follows:

$$\langle\Delta\epsilon_{\mathrm{EOE}}\rangle = \frac{\int dz\, \Delta\epsilon_{\mathrm{EOE}}(z)\cdot \mathrm{SW}(z)}{\int dz\, \mathrm{SW}(z)}, \tag{6}$$

amounting for this structure to -3.55×10^{-4}.

This anisotropy is aligned with the crystal axes defined in Fig. 2 and can interact with the misaligned anisotropy of the grating, effectively forming a 3D chiral cavity that induces elliptical polarization [13]. This phenomenon is confirmed by analyzing the calculated output Stokes parameters of the lasing polarization (see Eq. (1d)) and comparing them with measurements obtained for varying tilting angles ϕ_{grat}, as shown in Fig. 5. When $\phi_{\mathrm{grat}} = 0^\circ, 90^\circ, 180^\circ$, $S_3 = 0$, so the polarization is purely linear, as all anisotropies are aligned with crystal axes, while for intermediate angles, polarization is elliptical.

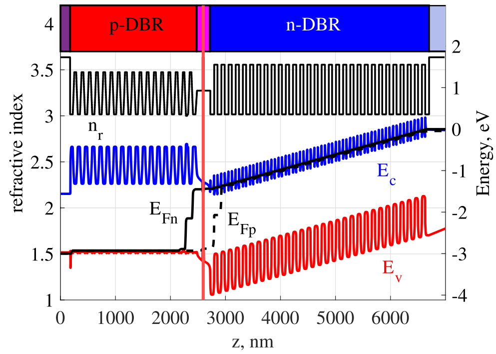

Fig. 3. Band diagram of the VCSEL together with the refractive index profile. The refractive index curve is read on the left axis, while all energies are read on the right axis. The vertical red line highlights the active region.

The excellent agreement between the computed and experimental Stokes parameters proves that VCSELs with SWG tilted to the crystal axes can emit elliptical polarization without modifying the state-of-the-art manufacturing processes. When strain is applied, the averaged anisotropy in Eq. (6) is modified, and it is possible to obtain a linear dependence as follows:

$$\begin{aligned}\langle\Delta\epsilon\rangle &= \frac{\int dz\, (\Delta\epsilon_{\mathrm{EOE}}(z) + \Delta\epsilon_{\sigma}(z))\cdot \mathrm{SW}(z)}{\int dz\, \mathrm{SW}(z)} = \\ &= \langle\Delta\epsilon_{\mathrm{EOE}}\rangle + \sigma\left(\frac{p_{44}}{2}\frac{\int dz\, n_r^4(z)\mathrm{SW}(z)}{\int dz\, \mathrm{SW}(z)}\right).\end{aligned} \tag{7}$$

For the device under study, it holds $\langle\Delta\epsilon\rangle = -3.55\times10^{-4} + 3.77\sigma$. This formula implies that the overall averaged intrinsic anisotropy can be zero when an external strain $\sigma_0 = 9.4\times10^{-5}$ is applied, thus eliminating the competition between the tilted grating anisotropy and the intrinsic ones. In this special case, the output polarization is always linear and oriented according to ϕ_{grat}. In secure data communication, protocols such as BB84 and the decoy state method [25] enable the use of VCSELs for quantum key distribution. The required different linear polarizations might be obtained realizing the specific strain σ_0 by applying an electrically induced strain [26].

Our model, as proved by the excellent comparison with the experimental results, allows to understand how lasing polarization depends on geometrical parameters such as ϕ_{grat}, t_{grat} and mechanically applied strain σ [26,27]. A simulation campaign is reported in Fig. 6. On the left map, the Stokes parameter S_3 is reported as a function of ϕ_{grat} and t_{grat}, reaching a large negative value for $t_{\mathrm{grat}} \simeq 310$ nm. Fixing this value, the right map displays the behavior of S_3 for varying ϕ_{grat} and σ, showing how a complete custom polarization control is possible in real-world standard grating VCSELs, including $S_3 = \pm1$ at the red stars. As expected from Eq. (7), $\sigma = \sigma_0$ implies $S_3 = 0$.

Conclusions. In this work, we theoretically and experimentally demonstrated how the interaction between tilted optical anisotropies enables VCSEL custom polarization states. Our results highlight the value of fast and efficient simulation campaigns in understanding how polarization depends on geometric and technological parameters, paving the way for the design of VCSELs with large S_3. A key advantage of this approach

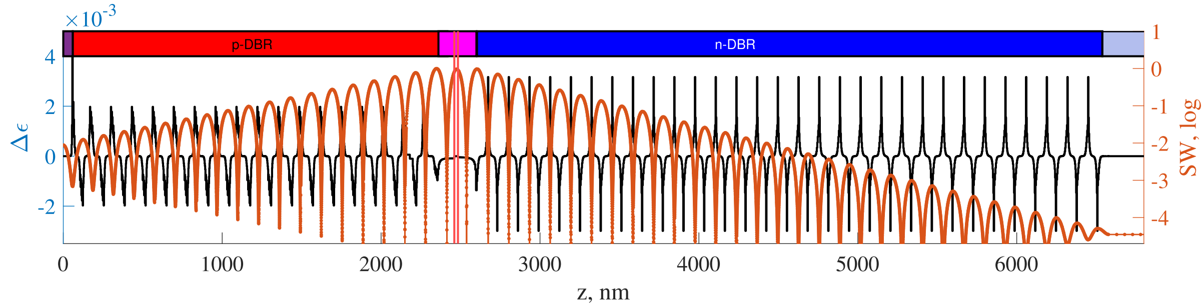

Fig. 4. SW and anisotropy profile resulting from the EOE, showing that only negative peaks of $\Delta\epsilon$ are relevant to the optical mode.

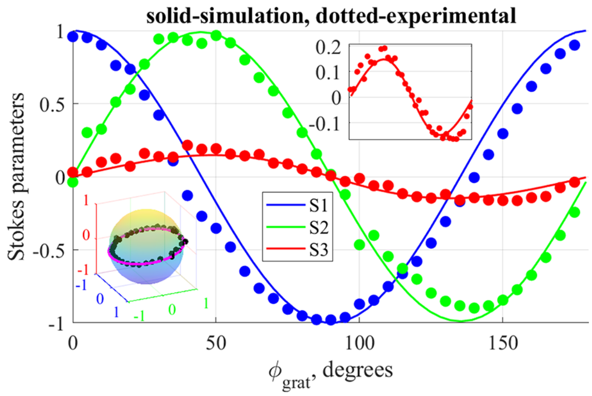

Fig. 5. Stokes parameters as a function of ϕ_{grat}, both simulated (solid) and experimental (dotted). Insets represent the Stokes parameters on the Poincaré sphere (bottom left) and a zoom of S_3 (top right).

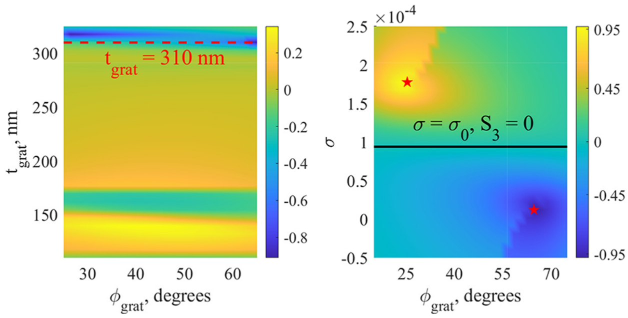

Fig. 6. Left: S_3 component of the lasing output polarization varying t_{grat} and ϕ_{grat}; the red dashed line is associated with the grating thickness for which S3 is the largest in magnitude. Right: S_3 component of the output polarization varying σ and ϕ_{grat} keeping t_{grat} = 310 nm; the black solid line is associated with σ_0 and linear output polarization.

over other meta-structured chiral layers is its reliance on well-established grating VCSEL technology, ensuring compatibility with existing fabrication processes.

Funding. NRRP Program RESTART, Project RIGOLETTO (PE00000001); German Federal Ministry for Economical Affairs and Climate Action projects (i-FPS Phase 2 (FKZ.50YJ2204B), i-FPS Phase 2a (FKZ.50YH2404C).

Acknowledgment. We appreciate the discussion within the Center of Excellence (CoE) VCSELence Turin. We thank S. Vollmer for technical support with the MOVPE.

Disclosures. The authors declare no conflicts of interest.

Data availability. Data underlying the results presented in this paper are not publicly available at this time but may be obtained from the authors upon reasonable request.

REFERENCES

1. H.-T. Cheng, Y.-C. Yang, T.-H. Liu, *et al.*, Photonics **9**, 107 (2022).
2. M. D'Alessandro, V. Torrelli, F. Bertazzi, *et al.*, IEEE Photonics J. **16**, 0600807 (2024).
3. M. Dummer, K. Johnson, S. Rothwell, *et al.*, *Optical Interconnects XXI*, Vol. 11692 H. Schröder and R. T. Chen, eds., International Society for Optics and Photonics (SPIE, 2021), p. 116920C.
4. G. Pan, M. Xun, X. Zhou, *et al.*, Light: Sci. Appl. **13**, 229 (2024).
5. N. A. Maleev, S. A. Blokhin, M. A. Bobrov, *et al.*, Gyroscopy Navig. **9**, 177 (2018).
6. Y. Zhou, Y. Jia, X. Zhang, *et al.*, Opt. Express **30**, 8991 (2022).
7. L. S. Watkins, C. Ghosh, J.-F. Seurin, *et al.*, Proc. SPIE **9616**, 96160J (2015).
8. K. Jin, X. Geng, Z. Liang, *et al.*, MDPI Electron. **11**, 3666 (2022).
9. J. Kitching, Appl. Phys. Rev. **5**, 031302 (2018).
10. D. Liang, C. Zhang, P. Zhang, *et al.*, Nat. Commun. **15**, 7660 (2024).
11. V. Torrelli, A. Gullino, A. Tibaldi, *et al.*, IEEE Photonics J. **16**, 0600507 (2024).
12. J. M. Ostermann, P. Debernardi, C. Jalics, *et al.*, Proc. SPIE **5364**, 5364 (2004).
13. V. Torrelli, M. D'Alessandro, W. Elsäßer, *et al.*, Opt. Lett. **49**, 3773 (2024).
14. G. P. Bava, P. Debernardi, and L. Fratta, Phys. Rev. A **63**, 023816 (2001).
15. G. G. Stokes, Trans. Cambridge Philos. Soc. **9**, 399 (1852).
16. A. Molitor, S. Hartmann, and W. Elsässer, Opt. Lett. **37**, 4799 (2012).
17. M. G. Moharam and T. K. Gaylord, J. Opt. Soc. Am. **71**, 811 (1981).
18. L. Li, J. Opt. Soc. Am. A **13**, 1870 (1996).
19. P. Debernardi and G. P. Bava, Phys. Status Solidi A **188**, 967 (2001).
20. G. Sinatkas, T. Christopoulos, O. Tsilipakos, *et al.*, J. Appl. Phys. **130**, 010901 (2021).
21. S. Adachi ed., *Properties of Aluminium Gallium Arsenide*, EMIS Datareviews Series (INSPEC, 1993).
22. A. Gullino, A. Tibaldi, F. Bertazzi, *et al.*, MDPI Appl. Sci. **11**, 6908 (2021).
23. B. Schaefer, E. Collett, R. Smyth, *et al.*, Am. J. Phys. **75**, 163 (2007).
24. A. Molitor, P. Debernardi, S. Hartmann, *et al.*, Opt. Lett. **38**, 4777 (2013).
25. M. Zimmer, M. Birkhold, M. Jetter, *et al.*, *Vertical-Cavity Surface-Emitting Lasers XXVIII*, Vol. PC12904 C. Lei and K. D. Choquette, eds., International Society for Optics and Photonics (SPIE, 2024), p. PC1290402.
26. T. Pusch, M. Lindemann, N. C. Gerhardt, *et al.*, *Vertical-Cavity Surface-Emitting Lasers XXII, Vol. 10552* (SPIE, 2018), pp. 59–64.
27. T. Pusch, M. Lindemann, N. Gerhardt, *et al.*, Electron. Lett. **51**, 1600 (2015).